



VLT/MUSE Observations of SDSS J1029+2623: Toward a High-precision Strong Lensing Model*

Ana Acebron¹, Claudio Grillo¹, Pietro Bergamini², Amata Mercurio³, Piero Rosati^{2,4}, Gabriel Bartosch Caminha⁵, Paolo Tozzi⁶, Gabriel B. Brammer^{7,8}, Massimo Meneghetti^{2,9,10}, Andrea Morelli⁴, Mario Nonino¹¹, and Eros Vanzella²

¹ Dipartimento di Fisica, Università degli Studi di Milano, Via Celoria 16, I-20133 Milano, Italy; ana.acebron@uni.mi.it

² INAF—OAS, Osservatorio di Astrofisica e Scienza dello Spazio di Bologna, via Gobetti 93/3, I-40129 Bologna, Italy

³ INAF—Osservatorio Astronomico di Capodimonte, Via Moiariello 16, I-80131 Napoli, Italy

⁴ Dipartimento di Fisica e Scienze della Terra, Università degli Studi di Ferrara, via Saragat 1, I-44122 Ferrara, Italy

⁵ Max-Planck-Institut für Astrophysik, Karl-Schwarzschild-Str. 1, D-85748 Garching, Germany

⁶ INAF—Osservatorio Astrofisico di Arcetri, Largo E. Fermi 5, I-50125, Firenze, Italy

⁷ Cosmic Dawn Center (DAWN), Jagtvej 128, DK-2200 Copenhagen N, Denmark

⁸ Niels Bohr Institute, University of Copenhagen, Jagtvej 128, København N, DK-2200, Denmark

⁹ National Institute for Nuclear Physics, viale Berti Pichat 6/2, I-40127 Bologna, Italy

¹⁰ Division of Physics, Mathematics, & Astronomy, California Institute of Technology, Pasadena, CA 91125, USA

¹¹ INAF—Osservatorio Astronomico di Trieste, via G.B. Tiepolo 11, I-34131 Trieste, Italy

Received 2021 August 19; revised 2021 November 10; accepted 2021 November 23; published 2022 February 15

Abstract

We present a strong lensing analysis of the galaxy cluster SDSS J1029+2623 at $z = 0.588$, one of the few currently known lens clusters with multiple images of a background ($z = 2.1992$) quasar with a measured time delay. We use archival Hubble Space Telescope multiband imaging and new Multi Unit Spectroscopic Explorer follow-up spectroscopy to build an accurate lens mass model, a crucial step toward future cosmological applications. The spectroscopic data enable the secure identification of 57 cluster members and of two nearby perturbers along the line of sight. We estimate the inner kinematics of a subset of 20 cluster galaxies to calibrate the scaling relations parameterizing the sub-halo mass component. We also reliably determine the redshift of four multiply imaged sources, provide a tentative measurement for one system, and report the discovery of a new four-image system. The final catalog comprises 26 multiple images from seven background sources, spanning a wide redshift range, from 1.02 to 5.06. We present two parametric lens models, with slightly different cluster mass parameterizations. The observed positions of the multiple images are accurately reproduced within approximately $0''.2$, the three image positions of the quasar within only $\sim 0''.1$. We estimate a cluster projected total mass of $M(<300 \text{ kpc}) \sim 2.1 \times 10^{14} M_{\odot}$, with a statistical uncertainty of a few percent. Both models, which include a small galaxy close to one of the quasar images, predict magnitude differences and time delays between the quasar images that are consistent with the observations.

Unified Astronomy Thesaurus concepts: Galaxy clusters (584); Strong gravitational lensing (1643); Dark matter (353); Quasars (1319)

1. Introduction

In recent years, thanks to the increased precision in the measurements of the value of the Hubble constant (H_0), some tension has emerged between the estimates from local and early-universe probes (Riess et al. 2019, 2021; Planck Collaboration et al. 2020). This discrepancy (see Verde et al. 2019, for a review) may point to the presence of unknown systematic effects (Freedman et al. 2020) or toward a deviation from the standard flat Lambda cold dark matter (Λ CDM) model and therefore interesting new physics. However, an explanation for this discrepancy has yet to be found, making the exploration of additional independent, complementary and high-precision techniques fundamental.

Since Refsdal theoretically predicted that a strongly lensed supernova (SN) with measured time delays between its

multiple images could provide an independent way to measure the value of the Hubble constant (Refsdal 1964), this technique has been able to provide competitive estimates of the value of H_0 . However, given the rarity of lensed SNe (Kelly et al. 2015; Goobar et al. 2017; Rodney et al. 2021), the strong lensing (SL) time-delay method has been mostly exploited with quasars strongly lensed by galaxies. In particular, the H_0 Lenses in COSMOGRAIL's Wellspring (HOLiCOW) program (Suyu et al. 2017), together with the COSmological MONitoring of GRAVitational Lenses (COSMOGRAIL) program (e.g., Tewes et al. 2013; Bonvin et al. 2018; Courbin et al. 2018), have estimated the value of H_0 with a 2.4% precision from the joint analysis of six gravitationally lensed quasars with measured time delays (Birrer et al. 2019; Sluse et al. 2019; Wong et al. 2020).

Using time-varying sources strongly lensed by galaxy clusters (Inada et al. 2003; Oguri et al. 2013; Sharon et al. 2017; Grillo et al. 2020) is a complementary technique that remains largely unexploited. On the one hand, galaxy-scale systems are more common, require a simpler total mass modeling, and may be less affected by line-of sight mass structures. On the other hand, cluster-scale systems are less prone to the so-called mass-sheet and mass-slope degeneracies (see, e.g., Grillo et al. 2020), and the

* This work is based in large part on data collected at the ESO VLT (prog. ID 0102.A-0642(A)) and the NASA HST.

longer time delays allow for measurements with smaller relative uncertainties, which can reach a few percent precision.

On galaxy cluster scales, SN ‘‘Refsdal’’ was discovered by Kelly et al. (2015) to be strongly lensed by the Hubble Frontier Fields (Lotz et al. 2017) galaxy cluster MACS J1149.5+2223 (Grillo et al. 2016; Treu et al. 2016). By exploiting Multi Unit Spectroscopic Explorer (MUSE; Bacon et al. 2010, 2014) spectroscopic identifications of a large number of multiple images in MACS J1149.5+2223, Grillo et al. (2018) inferred the value of the Hubble constant from the first multiply imaged and spatially resolved SN Refsdal, using a full SL analysis including the SN measured time delays (Kelly et al. 2016; Rodney et al. 2016). These first results suggest that time delays in lens galaxy clusters will become an important and complementary tool to measure the expansion rate and the geometry of the universe.

As shown in Grillo et al. (2018, 2020), to take full advantage of such lens clusters (that yield measured time delays with a few percent precision) as cosmological probes, it is necessary to construct an accurate cluster total mass model. In that sense, MUSE spectroscopy, together with high-resolution Hubble Space Telescope (HST) imaging, has allowed in the past few years the development of high-precision SL mass models through the identification of a large number of multiple images (e.g., Richard et al. 2015; Kawamata et al. 2016; Caminha et al. 2017, 2019; Mahler et al. 2018; Jauzac et al. 2019, 2021; Lagattuta et al. 2019; Rescigno et al. 2020; Ghosh et al. 2021) and the use of the stellar kinematics of cluster galaxies (Bergamini et al. 2019, 2021; Granata et al. 2021; Pignataro et al. 2021).

In this work, we present a new SL model of the galaxy cluster SDSS J1029+2623, at a redshift of $z=0.588$, based on recent MUSE observations. SDSS J1029+2623, hereafter SDSS1029, is one of the few presently known lens clusters producing multiple images (three, labeled as A, B, and C) of a background ($z=2.1992$) quasar (Inada et al. 2006; Oguri et al. 2008, 2013) with a large maximum image separation of $\sim 22''5$ (Inada et al. 2006). SDSS1029 was discovered in the Sloan Digital Sky Survey Quasar Lens Search (Oguri et al. 2006; Inada et al. 2012), which is a large survey that followed-up gravitationally lensed quasars that were spectroscopically confirmed in the Sloan Digital Sky Survey (SDSS; York et al. 2000). The first SL analysis of the cluster, using deep multiband HST observations, was presented in Oguri et al. (2013), where they also identified several other plausible multiple-image systems, all lacking a spectroscopic confirmation.

Moreover, after a 5.4 yr long optical monitoring campaign, a time delay of 744 ± 10 days was measured between the images A and B of the lensed quasar (Fohlmeister et al. 2013). The claimed $\sim 1\%$ uncertainty in this time delay offers an excellent opportunity for testing the cosmological applications of lens galaxy clusters with multiply imaged, time-varying sources.

This paper is organized as follows. In Section 2, we describe the HST imaging and MUSE spectroscopic observations. Section 3 presents the selection of the multiple images and cluster members, as well as the adopted methodology for the SL modeling of SDSS1029. Our findings are presented and discussed in Section 4. Finally, our conclusions are summarized in Section 5.

Throughout the paper, we adopt the standard Λ CDM flat cosmological model with $H_0 = 70 \text{ km s}^{-1} \text{ Mpc}^{-1}$, $\Omega_m = 0.3$, and $\Omega_\Lambda = 0.7$. In this cosmology, $1''$ corresponds to a physical scale of 6.62 kpc at the cluster redshift ($z = 0.588$). Magnitudes

are quoted in the AB system. Statistical uncertainties are given as the 68% confidence interval unless otherwise noted.

2. Observations and Data

This section presents the photometric and spectroscopic data sets used in this work.

2.1. Hubble Space Telescope Imaging

We use archival HST multicolor imaging (GO-12195; P.I.: Oguri), from the Advanced Camera for Surveys (ACS) and the Wide Field Camera 3 (WFC3), taken between 2011 April and May. SDSS1029 was imaged with ACS/F475W (two orbits), ACS/F814W (three orbits), and WFC3/F160W (two orbits). A description of the observations and data-reduction process is detailed in Oguri et al. (2013). We extract the photometric catalogs by using the software SExtractor (Bertin & Arnouts 1996) in dual mode, with the F814W band as the detection image. We apply a two-step extraction technique. In a first step, the bright and extended sources are properly deblended using the *cold mode*, then we set the configuration parameters in *hot mode* in order to detect faint objects and to properly split close sources (see, e.g., Rix et al. 2004; Caldwell et al. 2008). Finally, we use GALFIT (Peng et al. 2010) to measure the magnitude values of 20 objects that are affected by the presence of bright close neighbors: 19 cluster galaxies and one foreground galaxy (see Tables 2 and C1).

2.2. Very Large Telescope/MUSE Spectroscopy

SDSS1029 was recently observed with the integral field spectrograph MUSE, mounted on the Very Large Telescope (VLT), under the program 0102.A-0642(A) (P.I.: C. Grillo). The data were acquired between 2019 March 8 and May 3. Targeting the cluster with a single pointing ($\sim 1 \text{ arcmin}^2$), a total of 12 exposures of 1440 s each were obtained, with a cumulative exposure time of 4.8 hr on target.

We use the standard reduction pipeline (version 2.6, Weilbacher et al. 2020) to process the raw exposures and create the final stacked data cube. All standard corrections (bias, flat field, etc.) and calibrations (flux and wavelength) are applied. Moreover, we use the *auto-calibration* method implemented in the pipeline to mitigate the slice-to-slice flux variations. Since the sky-subtraction performed by the pipeline is known to leave significant residuals, we also apply the Zurich Atmosphere Purge (Soto et al. 2016). During the inspection of each of the 12 exposures, we notice that in one case the guide star tracking failed, strongly degrading the image quality of this specific exposure. The final data cube is composed of 11 exposures, totaling 4.4 hr depth on target, has a field of view of $\sim 1'.1$ across (see the top panel of Figure 1) and covers the wavelength range 4750–9350 Å, with a resolution of $\sim 2.4 \text{ \AA}$. The data has a spatial pixel size of $0''.2$ and the FWHM measured from the white image is $0''.71$.

To measure the redshifts of all objects located in the MUSE field of view, we extract one-dimensional spectra of all sources with HST detections within a circular aperture of $0''.8$ radius. For faint galaxies, we use custom apertures based on their estimated morphology from the HST imaging. With the help of spectral template matching of different galaxies, as well as the identification of emission lines (such as O II, Balmer lines, Ly α , UV carbon lines, etc.), we build our redshift catalog. To each redshift measurement is then assigned a quality flag (QF), which quantifies

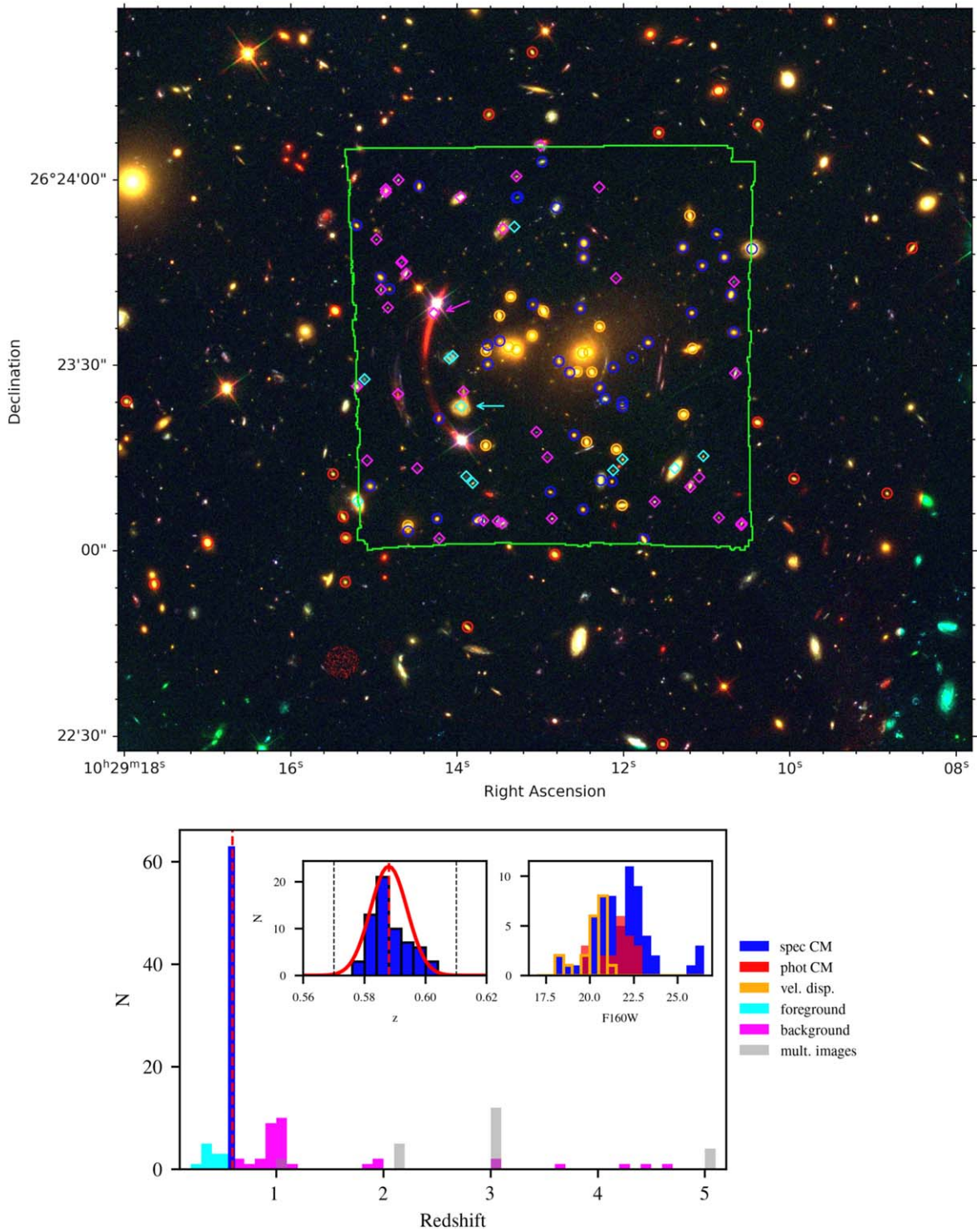


Figure 1. Top: Color-composite RGB image of SDSS1029, constructed with the HST/ACS passbands F435W (blue), F814W (green), and F160W (red). The MUSE footprint is shown in green. We show the spectroscopic and photometric cluster galaxies (as blue and red circles, respectively), and those with a reliable measurement of their stellar velocity dispersion (yellow circles). Foreground and background objects highlighted with arrows are included in the SL modeling as described in Sections 3.4 and 3.6. Bottom: MUSE spectroscopic redshift distribution of the objects identified ($QF \geq 2$) in the core of SDSS1029. The top left inset shows a zoom-in around the cluster redshift $z = 0.588$, as shown by the mean of the Gaussian (in red). The black dashed vertical lines locate the redshift interval $[0.57, 0.61]$, which includes the 63 spectroscopically confirmed MUSE cluster members (of which six objects have a $QF = 1$). The top-right inset shows the distribution of cluster members included in the SL modeling as a function of their magnitudes in the HST/F160W filter, following the same color-coding as in the top image.

its reliability (see Balestra et al. 2016; Caminha et al. 2016): *insecure* ($QF = 1$), *likely* ($QF = 2$), *secure* ($QF = 3$), and *based on a single emission line* ($QF = 9$).

The full spectroscopic sample contains 127 reliable (i.e., $QF \geq 2$) redshift measurements, of which one is a star, 12 are foreground ($z < 0.57$) galaxies, 57 are cluster members

Table 1
Coordinates and Spectroscopic Redshifts, with the Corresponding Quality Flag, of the Multiple-image Systems

ID ^a	R.A. (deg)	Decl. (deg)	z_{spec}	QF	ID
A	157.3081015	26.3883036	2.1992	3	1485
B	157.3093576	26.3944634	2.1992	3	1713
C	157.3095761	26.3939843	2.1992	3	1789
1.1	157.2980611	26.3907404	2.1778	1	2025
1.2	157.2978817	26.3924467	2.1778	1	2234
1.3	157.3008758	26.3974054	2.1778	1	2786
2.1	157.2981743	26.3915325	2.1812	2	1889
2.3	157.3014749	26.3977063	2.1812	3	2814
3.1	157.2990642	26.3923892	3.0275	3	2268
3.2	157.3074114	26.3913469	3.0275	3	2136
3.3	157.3041512	26.3982630	3.0275	3	2894
3.4	157.3015481	26.3880193	3.0275	3	1745
3.5	157.3017377	26.3879213	3.0275	3	1733
3.6	157.3018385	26.3878900	3.0275
3.7	157.3032208	26.3919632	3.0275	3	99992
4.1	157.2992278	26.3925219	3.0278	3	2286
4.2	157.3076382	26.3913247	3.0278	3	99994
4.3	157.3043869	26.3981437	3.0278	3	2877
4.4	157.3023985	26.3877048	3.0278
4.5	157.3035100	26.3920169	3.0278	3	99993
5.1	157.3019777	26.3946563	1.0232	3	2504
5.3	157.3008781	26.3917377	1.0232	3	2175
7.1	157.3075794	26.3951262	5.0622	3	99998
7.2	157.3064130	26.3960500	5.0622	3	99999
7.3	157.3014210	26.3936610	5.0622	3	999910
7.4	157.3012420	26.3938020	5.0622	3	999911

Note.

^a IDs are presented following the same notation as in Oguri et al. (2013).

($0.57 \leq z \leq 0.61$; see Section 3.1), 36 are background galaxies ($z > 0.61$), and 21 are multiple images (see Table 1). In particular, three high-redshift sources at $z = 4.23, 4.42, 4.66$ are identified. We also add six cluster members and three multiple images with $QF = 1$ after a visual inspection of their images and spectra. The foreground and background objects are shown in Figure 1 and their coordinates and redshifts are listed in Appendix B. The multiple images and cluster members catalogs are presented in Section 3.

3. Strong Lensing Modeling

We model the total mass distribution of SDSS1029 with the public software `lenstool`,¹² which adopts a parametric mass reconstruction (Kneib et al. 1996; Jullo et al. 2007). In this section, we present the multiple images used to optimize the model, the cluster-member selection, and a brief summary of the methodology. We refer to the publications mentioned above for further details (see, e.g., Caminha et al. 2016).

3.1. Cluster-member Selection

The cluster galaxies that are included in the SL model are selected based on both spectroscopic and photometric information.

First, we identify 57 galaxies with a reliable redshift estimate (i.e., with a $QF \geq 2$). Figure 1 shows the redshift distribution of these galaxies, which can be fit with a Gaussian distribution with mean and standard deviation values of $\bar{z} = 0.588 \pm 0.006$. We

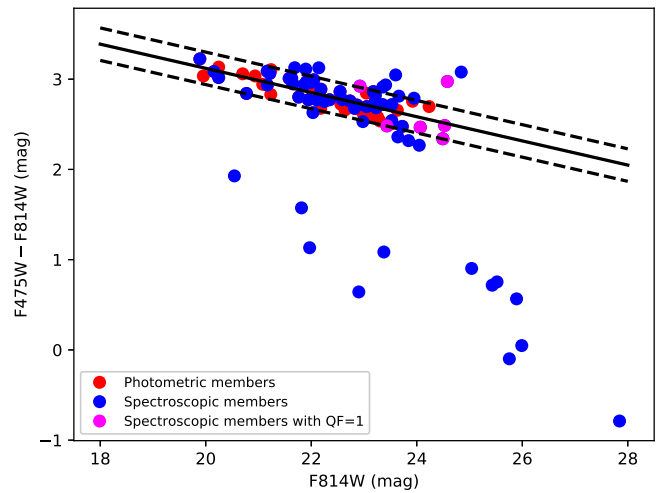


Figure 2. Color–magnitude relation of SDSS1029 spectroscopic members (blue dots). Red dots mark the photometrically selected cluster members, according to the red sequence, and the magenta dots are the spectroscopic members with $QF = 1$. The best fit of the spectroscopic red sequence is indicated in black, and the dashed lines represent the 68% confidence limits.

also identify six additional galaxies in the central region of the cluster with an uncertain redshift estimate ($QF = 1$), but bright enough ($F160W < 23.5$) to introduce significant perturbations to the overall lens model. These spectroscopic cluster members are selected as the galaxies with rest-frame relative velocities within $\Delta V = 3000 \text{ km s}^{-1}$ from the cluster mean velocity, which corresponds to the redshift range $z = 0.57\text{--}0.61$. We label as the two brightest cluster galaxies (BCGs) the two central galaxies (IDs 1933 and 1953 in Table C1). Each BCG has a close neighbor (within a projected distance of $\sim 1''.5$), which are identified in Table C1 as IDs 1964 and 1849, respectively. We complete the spectroscopic sample by selecting 20 additional photometric members lying on the cluster red sequence (see the red dots in Figure 2) and having $F160W \leq 24$. To determine the cluster red sequence, we fit the color–magnitude relation by considering all the spectroscopically confirmed member galaxies. The fit to the relation is obtained using the least-trimmed squares technique implemented by Cappellari et al. (2013). The black solid line in Figure 2 shows the red sequence, while the dashed lines indicate the 1σ measured scatter of 0.18.

Our final cluster-member catalog, including the 83 cluster-member galaxies that are integrated in the following lensing analysis, is presented in Figure 1, together with the galaxy redshift distribution and $F160W$ magnitudes. The complete catalog is also given in Appendix C, Table C1.

3.2. Multiple-image Systems

In this work, we consider both previous identifications of multiple-image systems available in the literature (Oguri et al. 2013), and a new system, discovered from an inspection of the HST images and the MUSE data cube.

The first system lensed by SDSS1029 to be identified was the triply imaged quasar (Inada et al. 2006; Oguri et al. 2008), for which we provide an updated spectroscopic redshift of $z = 2.1992$ based on the MUSE data. We also provide the first spectroscopic confirmation of the remaining five lensed systems identified in Oguri et al. (2013), whose redshift values were originally optimized in the SL modeling. We note that the spectroscopic redshifts of the five systems are consistent with the corresponding 2σ redshift intervals predicted by the SL

¹² <https://projets.lam.fr/projects/lenstool>

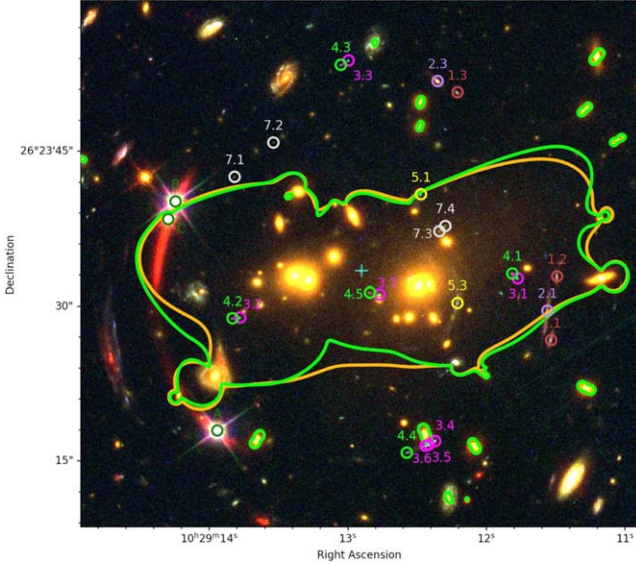


Figure 3. RGB image of the central region of SDSS1029, where several multiple images have been identified. We show here the images included in our SL models (listed in Table 1), following the same notation as in Oguri et al. (2013). The resulting critical curves at the quasar redshift ($z = 2.1992$) from our strong lensing best-fit Model 1 (in orange) and Model 2 (in green) are displayed. The cyan cross indicates the reference position from which the cumulative projected mass and average surface mass density profiles are computed.

model presented in Oguri et al. (2013). Moreover, we identify the new multiply imaged source 7, at a redshift $z = 5.0622$. The number and positions of four multiple images are well reproduced by our lens models. In addition to these confirmed four images, an extra, fainter image is predicted outside the MUSE field of view, in the southern region of the cluster. In our models, we decide not to consider families or images identified in Oguri et al. (2013) that do not have a clear emission peak in the HST photometry, namely system 6 and the individual images 2.2 and 5.2, since their positions cannot be estimated reliably.

All redshift measurements are classified as secure (QF = 3), but for image 2.1, which is classified as likely (QF = 2), and the three images of system 1 whose redshift estimate is considered unreliable (QF < 2). When all redshift measurements of a family have the same quality flag, we adopt the mean value of these measurements as the system redshift. On the other hand, as is the case for system 2, if different quality flags are available, we consider the most reliable one (i.e., a QF = 3) as the redshift of the system. In order to avoid biases on the determination of the cluster total mass, we consider in our lens models only multiple images with a secure spectroscopic confirmation (see, e.g., Grillo et al. 2015; Caminha et al. 2016; Johnson & Sharon 2016; Cerny et al. 2018; Remolina González et al. 2018). In the case of system 1, its redshift value is included as a free parameter, optimized during the lensing analysis, and the best-fit redshift value is found to be in agreement with the tentative spectroscopic measurement (see Section 4).

As all images have a HST detection, we carefully define the central position of each image as the luminosity peak in the HST F814W band.

The complete sample of multiple-image systems spans a large redshift range, between $z = 1.02$ and $z = 5.06$, with a total of 26 multiple images from seven background sources. We use

the observed positions of the multiple images as constraints in the lens models, providing in total 52 observables and 14 free parameters for the positions of the corresponding sources. We show the positions of the 26 multiple images in Figure 3 and their properties are summarized in Table 1. The extracted spectra for the objects with a QF ≥ 2 , with small cutouts of the HST color-composite image, are presented in Figure A1.

3.3. Modeling Methodology

We model the total mass distribution of SDSS1029 as the sum of several components: a diffuse mass component, representing the contribution of the dark matter and intra-cluster medium, together with small-scale halos, which account for the cluster galaxies (baryons and underlying dark matter).

The diffuse mass distribution is parametrized as a dual pseudo-isothermal elliptical mass profile (dPIE; Elíasdóttir et al. 2007). The free parameters associated with this profile are the following: the coordinates, x , y ; the ellipticity, defined as $\epsilon = (a^2 - b^2)/(a^2 + b^2)$, where a and b are the values of the major and minor semiaxes, respectively; the orientation, θ (counted counter-clockwise from the x -axis); the core and cut radii, r_{core} and r_{cut} ; and a velocity dispersion, σ_{LT} , which is related to the central velocity dispersion of the dPIE profile as $\sigma_0 = \sqrt{3/2} \sigma_{\text{LT}}$. The associated three-dimensional density distribution, as presented in Limousin et al. (2005), is defined as

$$\rho(r) = \frac{\rho_0}{(1 + r^2/r_{\text{core}}^2)(1 + r^2/r_{\text{cut}}^2)}, \quad (1)$$

where r is the distance from the center, and r_{core} and r_{cut} are the core radius and truncation radius, respectively. The dPIE density profile is characterized by two changes in the slope: within the transition region ($r_{\text{core}} < r < r_{\text{cut}}$), it behaves as an isothermal profile, where $\rho \propto r^{-2}$, while at larger radii, the profile falls more steeply, as $\rho \propto r^{-4}$.

On smaller scales, each halo associated with a cluster galaxy is modeled as a spherical dPIE with a vanishing core radius. In order to significantly reduce the number of free parameters in the modeling, the following scaling relations between the subhalo total mass and its associated luminosity (Jullo et al. 2007) are adopted:

$$\sigma_0 = \sigma_0^* \left(\frac{L}{L^*} \right)^\alpha, \quad (2)$$

$$r_{\text{cut}} = r_{\text{cut}}^* \left(\frac{L}{L^*} \right)^\beta, \quad (3)$$

where L^* is the reference luminosity of a galaxy at the cluster redshift, which we associate with the BCG (F160W = 18.24), σ_0^* and r_{cut}^* are the two parameters optimized in the lens analysis, and α and β represent the slopes of the σ_0 and r_{cut} scaling relations, respectively. As detailed in Bergamini et al. (2019, 2021; hereafter B19 and B21, respectively), we can define the total mass-to-light ratio as $M_i^{\text{tot}}/L_i \propto L_i^\gamma$, where the relation between the slope parameters can be expressed as $\beta = \gamma - 2\alpha + 1$. If $\gamma = 0.2$, the scaling relations are consistent with the so-called tilt of the fundamental plane (Faber et al. 1987; Bender et al. 1992).

Once the mass components are defined, described by a set of model parameters, \mathbf{p} , the best-fitting values of the model parameters are found by minimizing on the image plane the

Table 2

Foreground and Background Galaxies Included in the Strong Lens Modeling of SDSS1029

ID	R.A. ^a (deg)	Decl. ^a (deg)	F160W ^a (mag)	z_{spec}	QF
1625 ^b	157.308162	26.389775	17.03 ± 0.10	0.5111	3
999913 ^c	157.309500	26.393997	... ^d	0.6735	2

Notes.^a Coordinates and F160W magnitude (and associated error) are measured with Galfit.^b This galaxy is also referred to as FG in the text.^c This galaxy is also referred to as GX in the text.^d Being very close to the image C of the quasar, a reliable magnitude measurement could not be obtained.

distance between the observed, θ^{obs} , and model-predicted, θ^{pred} , positions of the multiple images. This is done by minimizing the χ^2 function, defined on the image plane as follows:

$$\chi^2(\mathbf{p}) = \sum_{j=1}^{N_{\text{fam}}} \sum_{i=1}^{N_{\text{img}}^j} \left(\frac{|\theta_{ij}^{\text{obs}} - \theta_{ij}^{\text{pred}}(\mathbf{p})|}{\sigma_{ij}} \right)^2, \quad (4)$$

where N_{fam} and N_{img}^j are the total number of families and images for the family, j , included in the modeling, respectively. The positional uncertainty for the observed images is σ_{ij} . We adopt an initial positional uncertainty of $0''.25$ for most images, but allow for a larger uncertainty, of $0''.5$, for the multiple images of families 2 and 5, as their exact positions are less reliably constrained. For the final model, the positional uncertainty is later rescaled in order to have a minimum χ^2 value comparable with the number of degrees of freedom (ν), i.e., to get $\chi^2/\nu \sim 1$.

Other statistical estimators are also used to assess the goodness of our reconstructions, in particular the rms value of the difference between the observed and model-predicted positions of the multiple images,

$$\text{rms} = \sqrt{\frac{1}{N_{\text{tot}}} \sum_{i=1}^{N_{\text{tot}}} |\theta_{ij}^{\text{obs}} - \theta_{ij}^{\text{pred}}(\mathbf{p})|^2}, \quad (5)$$

where N_{tot} is the total number of images. Finally, we consider the Bayesian information criterion (BIC; Schwarz 1978) and the corrected Akaike information criterion (AICc; Akaike 1974), which is suitable for models with a relatively low number of constraints. They are defined as follows:

$$\text{BIC} = -2 \ln(\mathcal{L}) + k \times \ln(n), \quad (6)$$

$$\text{AICc} = 2k - 2 \ln(\mathcal{L}) + \frac{2k(k+1)}{(n-k-1)}, \quad (7)$$

where \mathcal{L} is the maximum value of the likelihood (see Jullo et al. 2007), k is the number of free parameters, and n is the number of constraints.

3.4. A Bright Foreground and a Hidden Galaxy

This section provides a description of two galaxies, one in the foreground and one in the background of the cluster, that are included in the strong lens modeling, because of their vicinity in projection to the images A and C of the quasar. The properties of both objects are summarized in Table 2.

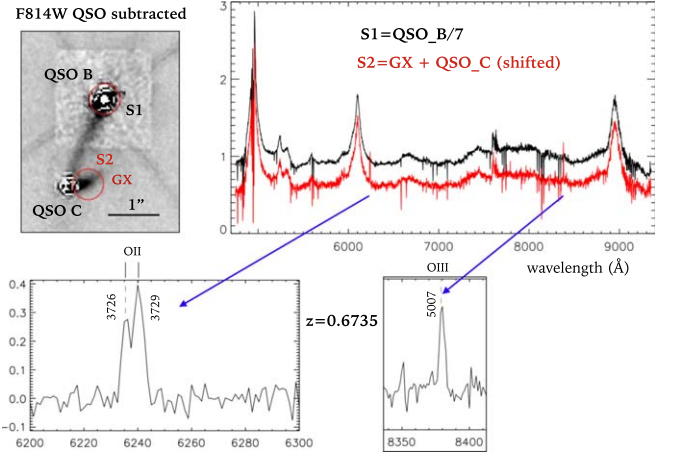


Figure 4. Top panel: MUSE one-dimensional spectra of the quasar (QSO) image B (S1 in black, rescaled by a factor of 7) and the hidden galaxy GX lying close to it, highly contaminated by the QSO image C (S2 in red). Both spectra are extracted from circular apertures of $0''.3$ radius, indicated in red in the HST F814W image cutout, where QSO B and C have been subtracted. Bottom panel: two portions of the subtracted one-dimensional spectrum ($S2-S1$), where the [O II] and [O III] emission lines of a source at a redshift of 0.6735 are highlighted.

The foreground ($z = 0.5111$) object is a bright spiral galaxy located $\sim 5''.3$ apart from the southern image A of the quasar (see Figure 3). We also include the galaxy that sits extremely close, at $\sim 0''.4$, to image C of the quasar and which was first identified in the HST images by Oguri et al. (2013), since it is known that substructures can affect the model-predicted values of time delays (Fohlmeister et al. 2007) and magnifications. Indeed, Oguri et al. (2013) showed that this galaxy, previously labeled as GX and considered in the lens model (at the cluster redshift), had a significant impact on the derived magnification of the quasar images, resolving the observed “flux ratio anomalies”.

Following an inspection of the MUSE data cube, we extract the spectrum of this object within a aperture of $0''.3$ radius, as shown in Figure 4. The obtained spectrum (S2) is affected by the contribution of both image C of the quasar and the perturber GX. We then subtract to it a properly rescaled spectrum of image B of the quasar (S1, which is not contaminated). The subtracted spectrum ($S2-S1$) clearly shows the [O II] $\lambda\lambda 3727, 3729$ Å doublet and the [O III] $\lambda\lambda 5007$ Å emission lines. We can then reliably measure a redshift of $z = 0.6735$, allowing us to confirm the background nature of the galaxy GX.

3.5. Internal Kinematics of Cluster Members

Extensive spectroscopic campaigns have allowed for a large number of multiple images to be identified, with measured spectroscopic redshifts. However, lens models still suffer from some degeneracies between the different mass components (Limousin et al. 2016). Indeed, differences between the scaling relations predicted by lens models without prior kinematic information and the measured line-of-sight stellar velocity dispersion for the cluster members have been previously reported for some well-studied clusters (B19). Such degeneracies can, however, be reduced when using additional independent information.

In this work, we use stellar kinematics from a subset of cluster members to better constrain the sub-halo population of the cluster. We follow the same methodology as in B19

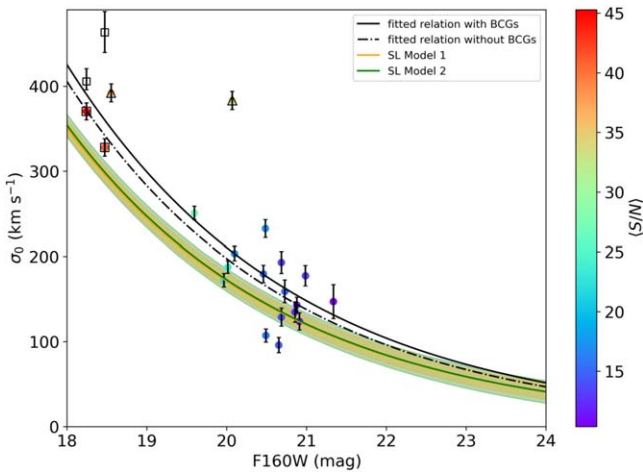


Figure 5. Measured stellar velocity dispersions of a subsample of 20 cluster members as a function of their magnitudes in the HST F160W filter (filled circles, whose colors depend on the $\langle S/N \rangle$ of their spectra). The black filled squares and triangles indicate the measurements of the four central galaxies. The black solid and dashed lines are the best-fit σ_0 -F160W relations, obtained as described in Section 3.5. The orange and green lines and areas correspond to the median and the 68% confidence level of the σ_0 -F160W relation from our SL Models 1 and 2, respectively. The resulting relations from the two lens models are consistent and do, in fact, overlap. We also mark as black empty squares the median velocity dispersions and associated 1σ uncertainties for the two BCGs, which are individually optimized in Model 2.

and B21. A detailed description of the methodology and comparison with simulations is given in these references, but we provide here a brief overview.

Spectra of all cluster members are extracted from the MUSE data cube within $0''.8$ radius apertures, which have shown to provide the best compromise between a high signal-to-noise ratio $\langle S/N \rangle$ value and a low contamination from the intra-cluster-light (ICL) or angularly close sources (the median FWHM value of these MUSE observations is $0''.71$; see Section 2.2). All the extracted spectra are then visually inspected, and if the contamination from the ICL is significant, the velocity dispersion of a faint galaxy is discarded, as it is likely biased high. To measure the line-of-sight stellar velocity dispersions, we use the public software Penalized Pixel-Fitting method (pPXF; Cappellari & Emsellem 2004; Cappellari 2017), and cross-correlate the observed spectra with an extended set of stellar templates in the rest-frame wavelength range $[3600, 5000]$ Å.

In order to only consider reliable line-of-sight velocity dispersion measurements, we follow the prescription adopted in B19 and B21, and we limit the sample to those galaxies with $\langle S/N \rangle > 10$ and $\sigma_0 > 80 \text{ km s}^{-1}$. The final sample of cluster members with measured velocity dispersions includes 20 objects down to F160W ~ 21 (see Figure 1). We also show in Figure 5 the measured velocity dispersion values as a function of the F160W magnitudes.

Following B19 and B21, we adopt a Bayesian approach to fit the measured velocity dispersions of the 20 cluster members. We can then derive the best-fit value of the slope α and the reference σ_0^* of the σ_0 -F160W relation. We note, however, that as the four central cluster galaxies of SDSS1029 (the two BCGs and two close neighbors; see Section 3) lie very close together (within $1''.5$; see Figures 1 and 3), their extracted spectra, from which the values of the stellar velocity dispersions are then measured, can be contaminated by their close neighbors, artificially increasing our

estimates. As illustrated in Figure 5, we perform two fits, including or not, these four central galaxies. We find that the resulting fits are very similar, with $\Delta\alpha \sim 0.01$ and $\Delta\sigma_0 \sim 20 \text{ km s}^{-1}$, the latter difference being included in the adopted measurement uncertainty. We choose to adopt in the following analysis the fit not including the four central galaxies. The posterior of the Bayesian fit is in turn used as a prior for the scaling relations in our strong lens models (see Section 3.6).

3.6. Mass Models

We consider several mass models in order to investigate which parameterization best reproduces the observed multiple image positions. We describe here two different and complementary SL models, *Model 1* and *Model 2*, hereafter. Both models adopt the same catalog of multiple images (with the same initial positional uncertainties) and cluster members, as presented in Sections 3.2 and 3.1. The redshift of system 1 is also optimized in both models, assuming a large flat prior.

Regarding the mass parameterization, both models include two large-scale dark matter (DM) halos, whose central coordinates are free to vary within $\pm 7''$ around the corresponding BCG positions. While the cut radius is fixed to a very large value, the ellipticity, position angle, core radius, and velocity dispersion are optimized within large flat priors. Cluster members are modeled within the scaling relations. Following the stellar velocity dispersion measurements for the subsample of cluster members presented in Section 3.5, we use a Gaussian prior for the value of the normalization σ_0^* centered on the measured value of 371 km s^{-1} , with a standard deviation of 91 km s^{-1} . A large prior for r_{cut}^* is adopted. We also fix the value of the slope α to the fitted value of 0.39 and we infer the value of β so that $M_i^{\text{tot}}/L_i \propto L_i^{0.2}$ (see Section 3.3). Both the foreground and the background (hidden) galaxy, GX, close to image C are also taken into account. These two line-of-sight mass structures are modeled at the cluster redshift, as a multiplane lensing framework is not yet fully implemented in the `lenstool` pipeline (Jullo et al. 2007). The two objects are then parametrized with a dPIE density profile, with their values of velocity dispersion and cut radius individually optimized in the lens model (i.e., outside of the scaling relations followed by the cluster members).

We summarize hereafter the differences between the two models.

- *Model 1.*

This model includes an external shear component, which brings the total number of free parameters related to the mass parameterization to 21. The external shear component (corresponding to a nonlocalized constant) helps to significantly improve the reproduction of the multiple images (see Section 4 and Table 3). The origin and impact of the external shear component is further discussed in Section 4.2.

- *Model 2.*

In this model, the two BCGs are individually parameterized (i.e., outside of the scaling relations): we consider them as spherical dPIEs with a vanishing core radius, and only their velocity dispersion and cut radius values are optimized, within large flat priors. This model has a total number of 23 free parameters related to the mass parameterization.

Table 3
Strong Lensing Mass Model Parameters for Model 1 (Top) and Model 2 (Bottom)

Model Statistics	Component	x ($''$)	y ($''$)	ϵ	θ (deg)	σ_0 (km s^{-1})	r_{cut} ($''$)	r_{core} ($''$)	γ_{ext}	ϕ (deg)
Rms = $0''.15$	DM_1953	$-12.5^{+0.6}_{-0.5}$	$2.8^{+0.2}_{-0.3}$	$0.63^{+0.05}_{-0.06}$	$1.6^{+3.7}_{-2.1}$	594^{+72}_{-28}	[2000]	$2.4^{+1.8}_{-1.0}$
$\chi^2/\nu = 0.71$	DM_1933	$2.2^{+0.5}_{-0.4}$	$0.3^{+0.4}_{-0.3}$	$0.66^{+0.04}_{-0.06}$	$36.3^{+1.8}_{-1.7}$	763^{+26}_{-39}	[2000]	$6.0^{+0.3}_{-0.5}$
$\log(\mathcal{L}) = 31.33$	1953	[-12.0]	[1.0]
$\log(\mathcal{E}) = -43.95$	1933	[0]	[0]
BIC = 75.63	FG	[-19.7]	[-8.8]	[0]	[0]	242^{+18}_{-18}	$20.0^{+0.2}_{-14.3}$	[0]
AIC = 7.34	GX	[-24.0]	[6.4]	[0]	[0]	58^{+24}_{-27}	$9.1^{+12.8}_{-0.3}$	[0]
AICc = 164.84	L^* Galaxy	322^{+10}_{-9}	$17.5^{+7.1}_{-4.1}$	[0]
	Ext. Shear	$0.09^{+0.02}_{-0.02}$	$65.9^{+4.4}_{-8.1}$
rms = $0''.22$	DM_1953	$-11.8^{+2.1}_{-4.0}$	$0.4^{+0.9}_{-1.2}$	$0.78^{+0.06}_{-0.08}$	$-4.6^{+2.9}_{-3.2}$	763^{+40}_{-54}	[2000]	$12.9^{+3.1}_{-1.9}$
$\chi^2/\nu = 1.03$	DM_1933	$5.5^{+0.6}_{-1.2}$	$4.1^{+1.0}_{-0.9}$	$0.63^{+0.06}_{-0.06}$	$32.6^{+4.0}_{-3.5}$	653^{+49}_{-45}	[2000]	$5.9^{+0.8}_{-0.8}$
$\log(\mathcal{L}) = 15.87$	1953	[-12.0]	[1.0]	[0]	[0]	463^{+25}_{-24}	$25.5^{+16.9}_{-9.0}$	[0]
$\log(\mathcal{E}) = -33.99$	1933	[0]	[0]	[0]	[0]	406^{+10}_{-15}	$16.5^{+2.4}_{-6.9}$	[0]
BIC = 114.46	FG	[-19.7]	[-8.8]	[0]	[0]	197^{+27}_{-48}	$17.6^{+4.5}_{-13.7}$	[0]
AIC = 42.26	GX	[-24.0]	[6.4]	[0]	[0]	78^{+23}_{-22}	$9.7^{+12.9}_{-0.4}$	[0]
AICc = 243.12	L^* Galaxy	325^{+13}_{-14}	$20.7^{+11.3}_{-6.5}$	[0]

Note. Median values and 68% confidence level intervals are quoted. Parameter values in square brackets are kept fixed.

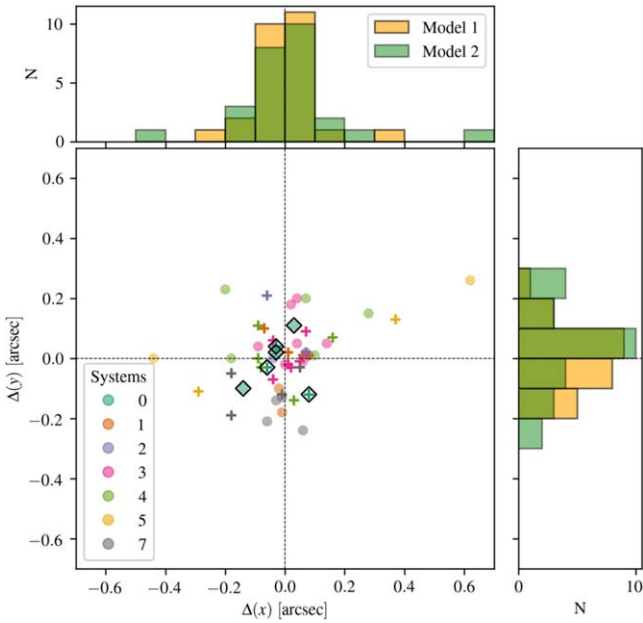


Figure 6. The middle panel shows the distribution of the separations $\Delta(x)$ and $\Delta(y)$ between the observed and model-predicted image positions as crosses (circles) for Model 1(2). The separations for the quasar images are, in addition, highlighted with black diamonds. The upper and right panels show the marginalized distributions of the $\Delta(x)$ and $\Delta(y)$ separations, respectively.

4. Results and Discussion

In this Section, we present the results of the two model optimizations. We also discuss the implications of adopting two different cluster total mass parameterizations on the model-predicted flux ratios and time delays between the quasar multiple images.

We show in Figure 6 the separations along the x - and y -axes between the model-predicted and observed image positions. We find that both models reproduce accurately the observed

positions of the multiple images with a resulting best-fit rms value of $0''.15(0''.22)$ for Model 1(2).

4.1. Mass Distribution

As described above, the cluster total mass distribution is composed of two cluster-scale DM halos centered around the two BCGs. The resulting median values of the parameters of the SL mass models, and the associated 1σ errors, are summarized in Table 3. The values of the statistical estimators introduced in Section 3.3 are also quoted. The values of the parameters of the two SL models are overall consistent within the uncertainties and, considering the values of all figures of merit, Model 1 is favored. In addition, the models predict for system 1 a redshift value of $z_{S1} = 2.17^{+0.02}_{-0.03}$ for Model 1 and $z_{S1} = 2.14^{+0.02}_{-0.03}$ for Model 2. These values are in agreement with each other, and with the tentative QF=1 redshift measurement provided by MUSE (see Table 1). We have checked that the difference in the resulting values of the positions, velocity dispersions, and core radii of the two cluster-scale halos in the two models can be explained by the degeneracy between the mass of the cluster-scale halos and of the two individually optimized BCGs. In detail, we have found that for the two different models the cumulative mass values projected within circular apertures of 100 kpc ($\sim 15''$) centered on the two BCGs are consistent, within the statistical uncertainties, despite the quite different contributions of the two most important mass components (i.e., the BCGs and the large-scale DM halos).

We show in Figure 7 the cumulative projected total (top panel) and the average surface mass density (bottom panel) profiles (not taking into account the two line-of-sight galaxies) as a function of the distance from the center of the cluster for both Model 1 (orange) and Model 2 (green). We also show the contribution from the sub-halo mass component as dashed lines. We measure a precise projected total cluster mass of $M(<300 \text{ kpc}) = 2.04^{+0.04}_{-0.03} \times 10^{14} M_{\odot}$ for Model 1 and $M(<300 \text{ kpc}) = 2.11^{+0.04}_{-0.03} \times 10^{14} M_{\odot}$ for Model 2. We find that these mass estimates are in agreement within the

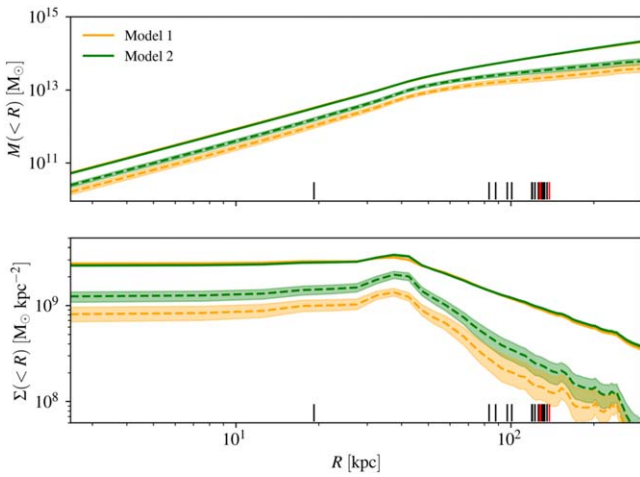


Figure 7. Top: cumulative projected mass profiles. Bottom: average surface mass density profiles. All profiles are plotted as a function of the distance (R) from the center of the cluster. The center is fixed at R.A. = $157^{\circ}303770$, decl. = $26^{\circ}392601$ (marked as a cyan cross in Figure 3) for the two SL models presented in this work. The colored solid lines show the median values of the total mass and surface mass density profiles, while the dashed lines correspond to the mass component associated to the sub-halos. The shaded areas encompass the 16th and the 84th percentiles, estimated from 500 random Bayesian Markov Chain Monte Carlo realizations. The projected distances of the 26 multiple images from the cluster center are marked with vertical black lines and the distances of the three images of the quasar are highlighted in red.

errors, and that the statistical uncertainty is approximately 2%. While the total cluster mass is precisely measured, the mass profile associated with the sub-halo component is significantly different between the two models. At a projected distance of 300 kpc from the cluster center, the sub-halo mass component represents approximately 20% and 30% of the cluster total mass for Models 1 and 2, respectively. The difference is driven by the different modeling of the two central BCGs, and therefore the resulting values of their velocity dispersions. Indeed, the mass associated with the cluster members modeled within the scaling relations is consistent between the two models within the 1σ uncertainties (as shown in Figure 5). The average surface mass density profiles shown in the bottom panel appear flat as they are computed from a reference center chosen between the two large-scale DM clumps (see Figure 3). We observe the same trend as for the mass profile, where the density profile associated with the sub-halo component is significantly different between the two models.

As displayed in Figure 8, we find an overall agreement between the two models on the derived total surface mass density distribution of SDSS1029. The differences can be explained by the different modeling of the BCGs in the most central regions and the inclusion of an external shear field in Model 1, which is discussed below.

4.2. On the Origin and Impact of the External Shear Field

As mentioned in Section 3.6, Model 1 requires a non-negligible external shear component (i.e., $\gamma_{\text{ext}} = 0.09$) to reproduce well the multiple image positions. Including an external shear term in SL models has proved to significantly improve the goodness of the reconstruction in specific cases (for a comparison of several different cluster mass parameterizations, see Caminha et al. 2019), e.g., in MACS J0329.7–0211 and RX J1347.5–1145 ($\gamma_{\text{ext}} = 0.07$ and $\gamma_{\text{ext}} = 0.10$, respectively; Caminha et al. 2019), MACS

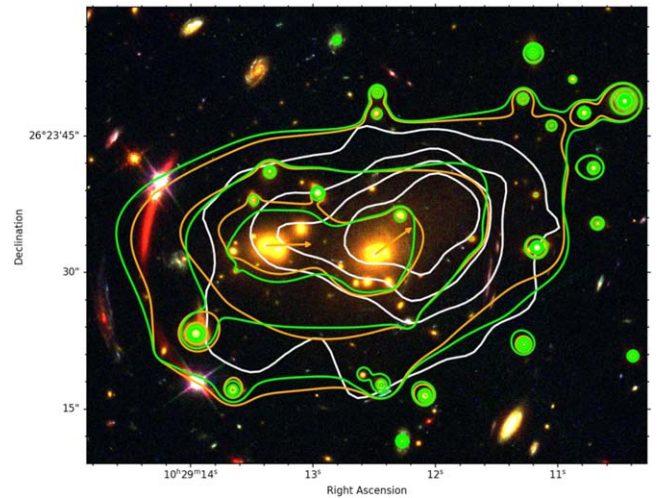


Figure 8. Color-composite image of the central region of SDSS1029, where we compare the contour levels of the total surface mass density distribution and the Chandra X-ray surface brightness (in white, after masking the strong emission from the three QSO images). Orange and green contours correspond, respectively, to the best-fit Models 1 and 2, and the levels are $[1.0, 1.5, 2.5] \times 10^9 M_{\odot} \text{ kpc}^{-2}$. The orange arrows indicate the orientation of the large-scale DM halos in Model 1.

J1206.2–0847 ($\gamma_{\text{ext}} = 0.12$; Caminha et al. 2016; Bergamini et al. 2019), A370 ($\gamma_{\text{ext}} = 0.13$; Lagattuta et al. 2019), and A2744 ($\gamma_{\text{ext}} = 0.17$; Mahler et al. 2018). This additional component can account for some significant lensing effects that would otherwise not be represented in the SL models. There are several possible reasons to include an external shear term in the SL modeling of SDSS1029.

SDSS1029 is a complex galaxy cluster with two main merging subclumps (see, e.g., Figure 8). The X-ray surface brightness obtained from Chandra observations (Observation ID: 11755) is centered near one of the BCGs (ID 1933 in Table 3) and is elongated in the east–west direction (Ota et al. 2012). This is illustrated in Figure 8, where we show the X-ray surface brightness contours obtained from the smoothed total band image (0.5–7 keV) from which the signal from the quasar multiple images has been subtracted. The image is obtained with a minimal Gaussian smoothing of $\sigma = 1''$. Ota et al. (2012) also identified a subpeak of X-ray emission northwest of the peak centered on the BCG with ID 1933, further supporting the merging scenario. Interestingly, we note that the large-scale DM halo associated with that BCG is oriented toward the X-ray emission subpeak in both SL models (see Figure 8). Recent studies have also found that massive structures at the redshift of a cluster but outside its central regions (Jauzac et al. 2016; Acebron et al. 2017; Mahler et al. 2018) or along the line of sight (McCully et al. 2017) can impact the mass reconstruction of the cluster core, an effect that can, however, vary significantly from cluster to cluster (Chirivì et al. 2018). This effect can be approximated with an external shear term. Finally, the sub-halos associated with the cluster members are parametrized in both our models with circular mass density profiles. The external shear component could also account for localized perturbations from non-modeled elliptical mass distributions.

We remark that the difference between our two SL models (see Table 3) in the derived ellipticity values of the two DM halos can be related to the external shear term. The inclusion of an external shear field in Model 1 results in rounder large-scale DM halos (see also Lagattuta et al. 2019). Specifically, the DM

Table 4
Values of Model-predicted Magnifications and Model-predicted and Observed Magnitude Differences between the Three Quasar Images

	Model 1 ^a	Model 1 w/o GX ^a	Model 2 ^a	Model 2 w/o GX ^a	Observations ^b
μ_A	$6.5_{-0.4}^{+0.4}$	$6.7_{-0.5}^{+0.4}$	$5.2_{-0.3}^{+0.4}$	$5.6_{-0.3}^{+0.3}$...
μ_B	$16.9_{-5.0}^{+6.4}$	$23.8_{-2.6}^{+3.9}$	$12.3_{-2.9}^{+5.8}$	$24.6_{-3.5}^{+4.4}$...
μ_C	$5.6_{-3.0}^{+12.6}$	$24.6_{-2.8}^{+4.1}$	$3.0_{-1.2}^{+5.7}$	$25.8_{-3.7}^{+4.5}$...
$\Delta\text{mag(AB)}$	$1.0_{-0.3}^{+0.3}$	$1.4_{-0.2}^{+0.2}$	$0.9_{-0.2}^{+0.4}$	$1.6_{-0.2}^{+0.2}$	0.36 ± 0.02
$\Delta\text{mag(BC)}$	$-1.2_{-0.4}^{+1.1}$	$0.0_{-0.1}^{+0.1}$	$-1.6_{-0.3}^{+0.9}$	$0.0_{-0.1}^{+0.1}$	-1.96 ± 0.05
$\Delta\text{mag(AC)}$	$-0.2_{-0.8}^{+1.2}$	$1.4_{-0.2}^{+0.2}$	$-0.6_{-0.5}^{+1.1}$	$1.7_{-0.2}^{+0.2}$	-1.60 ± 0.05

Notes.

^a The median magnification estimates and associated 1σ uncertainties are computed at the model-predicted positions of the multiple images from a subset of 500 Markov Chain Monte Carlo random realizations.

^b Based on magnitudes in the G band from the Gaia EDR3 catalog, which are $\text{mag}(A) = 18.67$, $\text{mag}(B) = 18.31$, and $\text{mag}(C) = 20.27$.

halos associated with the BCG with ID 1933 have ellipticity values that are consistent, given the statistical uncertainties, while the DM halo associated with the BCG with ID 1953 has an ellipticity value $\sim 20\%$ larger in Model 2 (i.e., when the external shear term is not present).

4.3. On the Multiply Imaged Quasar System

The three quasar images form the most interesting system lensed by SDSS1029. Both models reproduce well the positions of the quasar multiple images, with best-fit rms values of $\sim 0.1''$ for this system. We note that our current SL models do only include the observed positions of the quasar multiple images as observational constraints. We delegate to future work the inclusion of the observed quasar image flux ratios and time delays and the detailed modeling of the surface brightness of the quasar host galaxy (Suyu & Halkola 2010; Monna et al. 2015, 2017).

This system is also of particular interest due to the observed flux ratio anomalies. As pointed out in Oguri et al. (2013), preliminary lens models would predict similar magnitudes for the images B and C (which lie close together and close to the tangential critical curve; see Figure 3), while image A would appear fainter (i.e., $\mu_A < \mu_B \sim \mu_C$). However, we observe $\mu_A \sim \mu_B > \mu_C$. We show in Table 4 the model-predicted magnification values (estimated at the model-predicted image positions) together with the observed and model-predicted magnitude differences between couples of quasar images for both models, computed as $\Delta\text{mag}(XY) = -2.5 \log\left(\frac{\mu_X}{\mu_Y}\right)$. The observed magnitudes are the G -band mean values from the Gaia EDR3 public catalog, and we associate a typical error of 0.01 mag in the G -magnitude range ≈ 18 –20 (Riello et al. 2021), appropriate for the images A, B, and C. To quantify the impact of the background small galaxy GX, we also present the model-predicted magnification values and magnitude differences when the potential associated with this galaxy is not included in the models, therefore fully taking into account how a model would compensate for the absence of GX with the other cluster mass components. In Figure 9, we display the best-fit absolute magnification map computed at the quasar redshift, and the map ratio between the two models. The magnification of image A has a low relative error, as it is located far from the critical curves, and both models predict a magnification value lower than that of image B. On the other hand, the relative errors for images B and C are significantly larger since they are close to the tangential critical curve (Meneghetti et al. 2017). In particular, predicting a precise magnification estimate for image C is a complex

undertaking, due to its closeness to both the critical curve and the background perturber. Within the uncertainties, our magnification values are in agreement with the best-fit estimates quoted in Oguri et al. (2013) for their SL model including the hidden galaxy. We also find that the observed and model-predicted magnitude differences are consistent within 2σ for both models, with Model 2 being slightly in better agreement with the observations. In order to get a predicted magnitude difference between the images B and C ($\Delta\text{mag(BC)}$) in agreement with the observations, the inclusion of the hidden background galaxy is crucial, comparable to the finding reported in Oguri et al. (2013). In addition, Rojas et al. (2020) recently found no evidence of microlensing for this system. However, in contrast with the SL model presented in Oguri et al. (2013), we do not find that the inclusion of the GX substructure has an impact on the model-predicted magnification value for image A. GX has, however, a significant impact on the model-predicted magnitude differences between images A and B, and A and C (see Table 4), resolving in part the observed ‘‘anomaly’’. A possible scenario to explain the remaining differences between the model-predicted and observed values of $\Delta\text{mag(AB)}$ and $\Delta\text{mag(AC)}$ is the intrinsic variability of the source coupled with the time delays between the images. As shown by the light curves of images A and B+C combined (see Figure 4 in Fohlmeister et al. 2013), the background quasar appears as a significantly variable source, with a maximum $\Delta\text{mag} \sim 0.7$ mag. Since the magnitudes of the multiple images of the quasar are measured from observations taken at the same time, but, because of the time delays, the corresponding emission times for the source are different, this could produce observed magnitude differences between the images of several tenths of magnitude.

Finally, we provide some discussion on the predicted time delays between the images A and B, Δt_{AB} , and between the images B and C, Δt_{BC} . We use 500 random Markov Chain Monte Carlo realizations from our SL models to estimate the median time delay between each couple of images (computed at the model-predicted image positions) and the 1σ associated errors. We find time-delay values of $\Delta t_{AB} = 740_{-210}^{+182}$ days and $\Delta t_{BC} = 5_{-3}^{+3}$ days for Model 1. Regarding Model 2, we find $\Delta t_{AB} = 928_{-198}^{+200}$ days and $\Delta t_{BC} = 9_{-4}^{+6}$ days. Both model predictions of Δt_{AB} are thus in agreement with the measured time delay of 744 ± 10 days (Fohlmeister et al. 2013) within the 1σ uncertainties. We also find that not including the local perturber GX in the SL models yields consistent, within the statistical uncertainties, Δt_{AB} values with respect to the fiducial Models 1 and 2. Only the model-predicted Δt_{BC} value

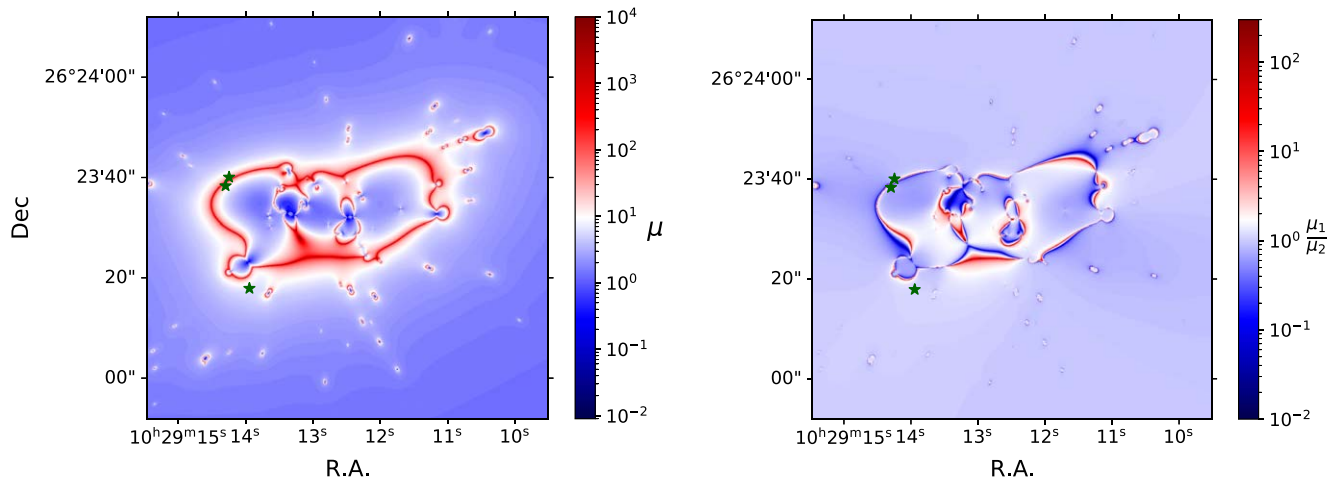


Figure 9. Left: absolute magnification map of SDSS1029 from our best-fit Model 1 for a source at the quasar redshift $z = 2.1992$. Right: magnification map ratio between the best-fit Models 1 and 2. In both panels, the green stars mark the observed positions of the three quasar images.

significantly decreases with respect to the model-predicted values for Models 1 and 2, which can be explained by the fact that the light rays traveling from the source to us are not pulled in the GX gravitational potential, and can reach us in a shorter amount of time.

It is worth noting that two very similar cluster lens models (which estimate the same cluster total mass within $\sim 2\%$, and reproduce equally well the positions of the quasar images) predict values of the Δt_{AB} time delay that differ by approximately 25%, which would in turn provide significantly different H_0 estimates. As previously mentioned, SDSS1029 presents a complex total mass distribution, with two merging mass components and a background perturber close to image C. As shown also in this work, perturbations introduced by substructures can have a significant impact on the predicted flux ratios and time delays between the quasar images (see also Oguri 2007; Keeton & Moustakas 2009). Furthermore, the quasar multiple images belong to the outermost SL system identified in the field, in a region where no other multiple images are seen.

We remark that the results presented in Grillo et al. (2020) show that accurate and precise measurements of the values of the cosmological parameters through time-delay cluster lensing require SL models that include the measured values and uncertainties of the multiple-image time delays as observational constraints. As proved also here, to be competitive with other cosmological probes, it is not possible to use or combine the time-delay predictions obtained from different lens models that exploit only the observed positions of a set of multiple images (i.e., not including the measured time delays as observables).

Another interesting aspect in SDSS1029 comes from the quasar host galaxy, which is lensed into a giant, $\sim 27''$ long tangential arc (see Figure 3). In a future work, we plan to go beyond *point-like* SL models and reconstruct the surface brightness of the arc. This will grant us a much larger number of observational constraints, which will be used in combination with the measured time delays, to improve the accuracy and precision of our SL models for proper cosmological applications.

5. Conclusions

In this work, we have presented a new parametric SL model of the galaxy cluster SDSS J1029+2623 at $z = 0.588$, which is

one of the few currently known lens clusters hosting a multiply imaged background quasar. We have exploited recent spectroscopic observations taken with MUSE in combination with archival HST imaging to securely identify multiple images and cluster galaxies. We have used the new spectroscopic data to perform some accurate strong lens modeling of the cluster with the `lenstool` pipeline (Jullo et al. 2007). Our main results are the following:

1. We have spectroscopically confirmed four multiple-image systems, which were previously identified based solely on photometric information. We have provided an updated redshift for the quasar and a tentative redshift for one system, which is in excellent agreement with the redshift predictions from our SL models. We have discovered a new system consisting of four multiple images at a redshift of $z = 5.0622$, the highest redshift of our sample. In total, our SL models have included seven families spanning a large redshift range between 1.0 and 5.1, with a total of 26 multiples images (see Table 1 and Figures 3 and A1).
2. We have spectroscopically confirmed 63 cluster galaxies: 57 objects have been reliably identified with a $QF \geq 2$ and six additional objects have a $QF = 1$ and colors that make them reliable identifications. In addition, we have completed our spectroscopic catalog with a subset of member candidates outside the MUSE field of view, which were selected on the basis of their multiwavelength photometric information (see Table C1 and Figure 2).
3. We have exploited the new MUSE spectra to measure the central stellar kinematics of a subsample of 20 cluster members down to $F160W \sim 21$. The measured values of the stellar velocity dispersions have been in turn used to better constrain the scaling relations of the sub-halo population in the lensing models (see Figure 5).
4. We have confirmed the background nature of the hidden galaxy GX, angularly very close to image C of the quasar, at a redshift $z = 0.6735$ (see Figure 4).
5. We have presented two slightly different lens models that accurately reproduce the positions of all multiple images used as constraints, with rms values of the difference between the model-predicted and observed image positions of $0''.15(0''.22)$ for Model 1(2). In particular, the

positions of the three quasar images are reproduced with a mean rms value of only $\sim 0''.1$ in both models.

6. We have measured a cluster projected total mass value of $M(<300 \text{ kpc}) \sim 2.1 \times 10^{14} M_{\odot}$ for both models, with a relative statistical uncertainty of approximately 2%.
7. We have confirmed, as previously stated in Oguri et al. (2013), that the inclusion of the hidden galaxy GX in the lens model resolves the flux ratio anomaly between images B and C. Those between images A and B/C, instead, could not be fully resolved with GX only. The intrinsic variability of the source, coupled with the time delays between the images, might explain the remaining flux differences.
8. Within the uncertainties, both SL models predict time delays between images A and B that are consistent with the measured value presented in Fohlmeister et al. (2013). We emphasize that these predictions should not be used to infer the value and uncertainty of the Hubble constant, since the measured time delay has not yet been included as an observational constraint in the models (which are optimized only with the observed positions of the multiple images).

SDSS J1029+2623 is a complex merging cluster. In order to fully take advantage of the measured time delay between images A and B (with a remarkable 1% relative error) for cosmological applications, all available lensing observables will be incorporated in future strong lens models. Toward this end, we plan to use the GLEE software (Suyu & Halkola 2010; Suyu et al. 2012), which offers the opportunity to add as observational constraints in the SL modeling both the measured time delay, Δt_{AB} , and the surface brightness distribution of the multiple images of the quasar host galaxy.

The full MUSE spectroscopic catalog of SDSS J1029+2623 presented here has been made publicly available.¹³

We kindly thank the referee for the insightful and useful comments received. We acknowledge financial support through grant PRIN-MIUR 2017WSCC32: “Zooming into dark matter and proto-galaxies with massive lensing clusters”. A.A warmly thanks S. H. Suyu for her useful and constructive comments. G. B.C. thanks the Max Planck Society for support through the Max Planck Research Group for S. H. Suyu and the academic support from the German Centre for Cosmological Lensing.

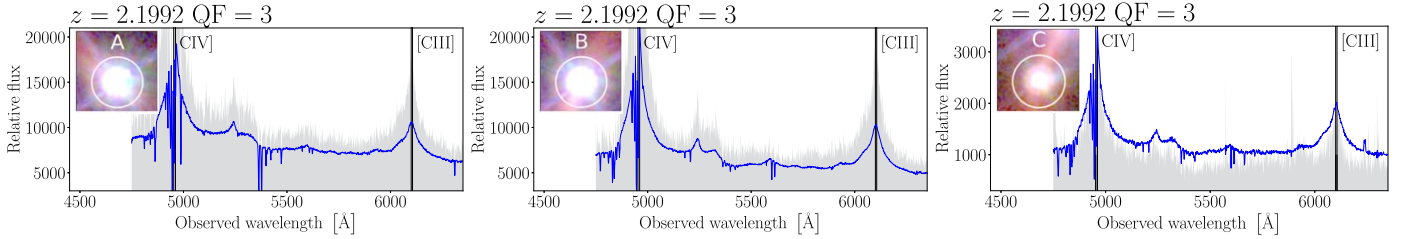
Facilities: HST(ACS, WFC3), VLT(MUSE).

¹³ The catalog is available at www.fe.infn.it/astro/lensing.

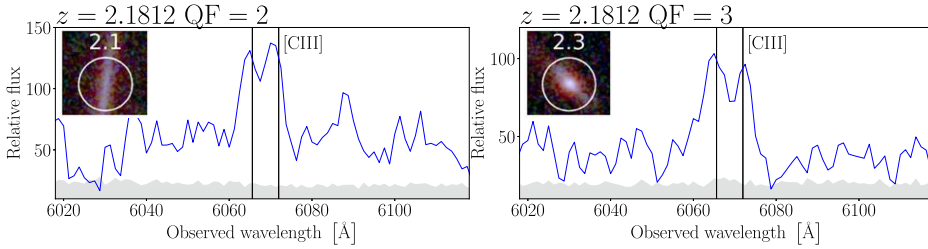
Appendix A Multiple Images

Appendix A presents in Figure A1 the MUSE data of the multiple images identified in SDSS1029 with a secure redshift quality flag of $QF > 2$.

Family QSO



Family 2



Family 3

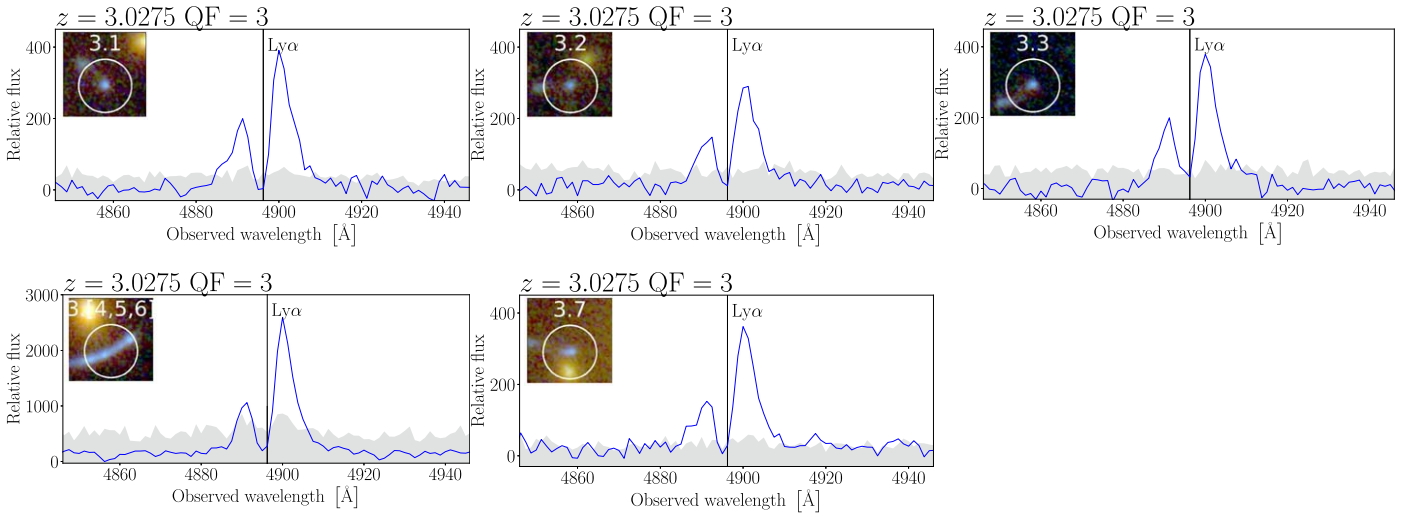
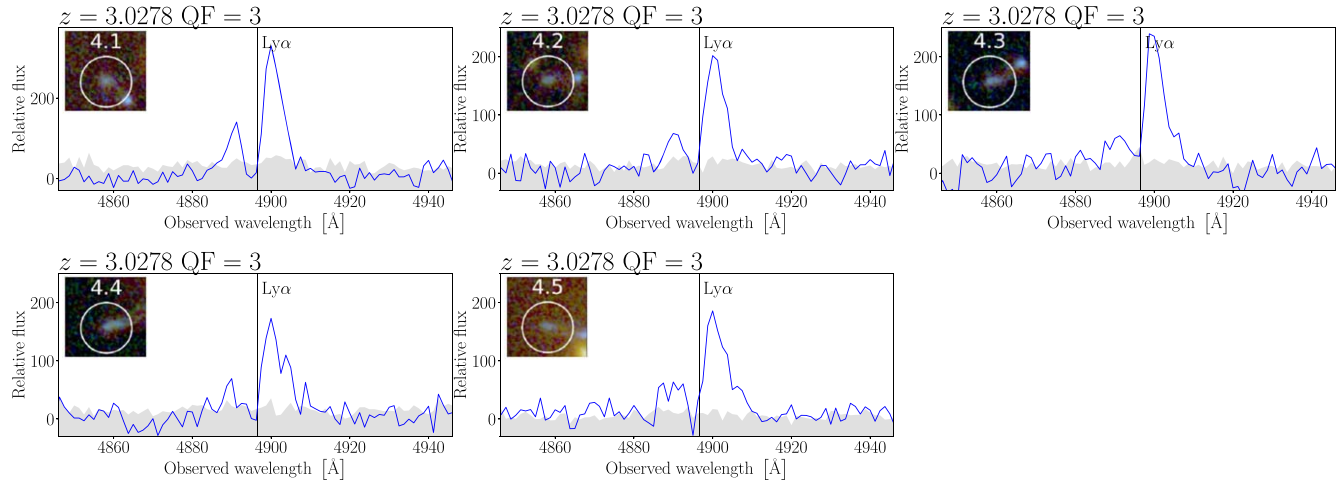
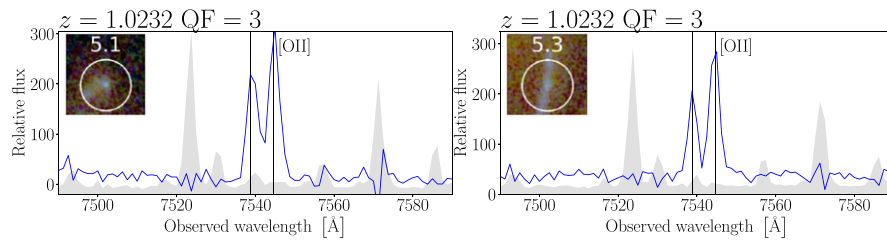


Figure A1. MUSE data of the multiply imaged background sources identified in SDSS1029. The vertical black lines indicate the positions of the emission lines based on the best estimate of the systemic redshift. The gray area shows the rescaled variance obtained from the data-reduction pipeline. The flux is given in units of $10 \text{ erg s}^{-1} \text{ cm}^{-2} \text{ \AA}^{-1}$. The image cutouts in each panel are extracted from the color-composite HST image and are $2''$ across. The white circles show the HST counterparts.

Family 4



Family 5



Family 7

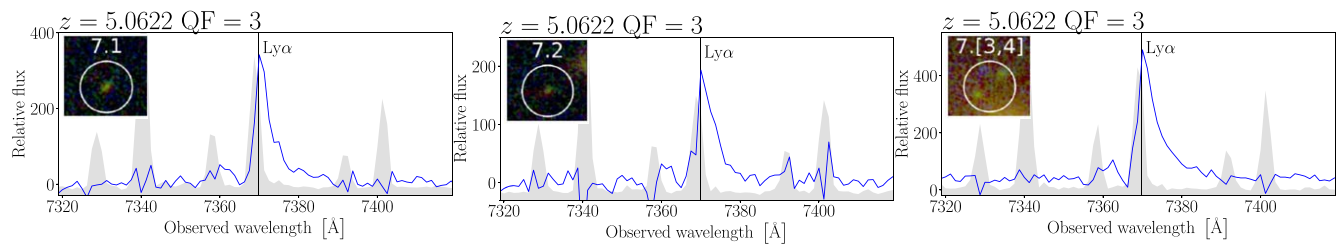


Figure A1. (Continued.)

Appendix B

Foreground and Background Sources from MUSE

Appendix B presents in Table B1 the redshift catalog of the foreground and background sources identified within the MUSE field of view.

Table B1
Catalog of the Spectroscopically Identified Objects within the MUSE Field-of-view Pointed at SDSS1029

ID	R.A. (deg)	Decl. (deg)	z_{spec}	QF
1241	157.297428	26.387029	0.4085	3
1261	157.313315	26.385537	0.3396	3
1546	157.307545	26.386366	0.3419	3
1606	157.300511	26.386937	0.3407	3
1625	157.308160	26.389774	0.5111	3
1674	157.300040	26.387435	0.3611	3
1688	157.296005	26.387573	0.4080	3
2056	157.312978	26.391023	0.2936	3
2082	157.308720	26.391958	0.5120	3
2207	157.308551	26.392061	0.5120	3
99991	157.305466	26.397866	0.4869	9
999912	157.307886	26.386664	0.3419	2
1299	157.3092241	26.3838706	1.0299	3
1301	157.306078	26.384555	1.0229	3
1360	157.307012	26.384687	0.9078	3
1362	157.294096	26.384484	0.9075	3
1368	157.294083	26.384561	0.9075	3
1381	157.306315	26.384649	1.0233	3
1391	157.303578	26.384776	1.0240	3
1394	157.295228	26.384820	0.9272	3
1460	157.298442	26.385533	1.9781	2
1528	157.296660	26.386191	1.0965	3
1621	157.310328	26.387028	0.8840	9
1665	157.312845	26.387381	4.2281	3
1685	157.303819	26.387522	1.0881	9
1802	157.304357	26.388654	1.1130	9
1978	157.313342	26.390708	1.0036	3
2006	157.311295	26.390369	1.9094	2
2031	157.294407	26.391291	0.9190	3
2453	157.311805	26.394246	0.6640	3
2518	157.312155	26.395054	0.7227	3
2571	157.310895	26.395766	1.8942	3
2585	157.306033	26.397789	0.9390	3
2594	157.294471	26.395405	0.9183	3
2610	157.300366	26.395570	0.9177	3
2684	157.311124	26.396271	3.0296	3
2688	157.311085	26.396321	3.0296	3
2773	157.312375	26.397311	3.6651	2
2875	157.308164	26.399206	0.8168	3
2952	157.311901	26.399437	1.0892	3
3010	157.311906	26.399559	1.0894	3
3020	157.301205	26.399645	4.6553	3
3054	157.311282	26.399976	1.0887	3
3069	157.305358	26.400140	1.0579	3
3128	157.304154	26.401516	0.6736	2
99996	157.308018	26.390477	0.9170	3
99997	157.296211	26.386627	4.4242	3
999913	157.309500	26.393997	0.6735	2

Note. We present foreground and background objects in the top and bottom panels, respectively. All listed coordinates are estimated with `SExtractor` based on the F814W band as detection image.

Appendix C Cluster Members

Appendix C presents in Table C1 the redshift and F160W magnitude catalog of the cluster members included in the SL modeling of SDSS1029.

Table C1

Catalog of the Spectroscopic (Top) and Photometric (Bottom) Cluster Members Included in the SL Modeling of SDSS1029

ID	R.A. (deg)	Decl. (deg)	F160W (mag)	z_{spec}	QF
1933 ^a	157.302047	26.392209	18.24 ± 0.10	0.5853	3
1953 ^a	157.305754	26.392473	18.47 ± 0.10	0.5959	3
1849 ^a	157.305350	26.392348	18.55 ± 0.10	0.6017	3
2567 ^a	157.293560	26.396878	19.36 ± 0.10	0.5877	3
2170 ^b	157.296543	26.392404	19.60 ± 0.03	0.5914	3
1936 ^b	157.304575	26.392983	19.97 ± 0.04	0.5976	3
2336 ^b	157.304008	26.394089	20.02 ± 0.04	0.5858	3
1964 ^a	157.301731	26.392245	20.07 ± 0.10	0.5868	2
1286 ^a	157.310804	26.384452	20.10 ± 0.10	0.5987	3
2705 ^b	157.296677	26.398377	20.46 ± 0.05	0.5868	3
2321 ^b	157.301195	26.393396	20.49 ± 0.05	0.5864	3
2404 ^b	157.305649	26.394742	20.49 ± 0.05	0.5802	3
1833 ^b	157.296993	26.389444	20.65 ± 0.05	0.5865	3
1655 ^b	157.300360	26.387879	20.69 ± 0.06	0.5821	3
1645 ^b	157.301848	26.388213	20.69 ± 0.06	0.5841	3
2090 ^b	157.302317	26.391371	20.73 ± 0.06	0.5881	3
2335 ^b	157.306216	26.393884	20.86 ± 0.06	0.5921	3
1414 ^b	157.300071	26.385367	20.88 ± 0.06	0.5799	3
1692 ^b	157.306902	26.388058	20.91 ± 0.06	0.5899	3
2076 ^b	157.301588	26.391352	20.99 ± 0.06	0.5862	3
1399 ^a	157.301142	26.386493	21.07 ± 0.10	0.5878	3
1337 ^a	157.307290	26.384720	21.08 ± 0.10	0.5929	3
2424 ^b	157.294615	26.394830	21.11 ± 0.07	0.5850	3
1253 ^b	157.298980	26.383842	21.13 ± 0.07	0.5771	3
2701 ^b	157.301987	26.397147	21.22 ± 0.07	0.6002	3
2141 ^b	157.306888	26.392297	21.34 ± 0.08	0.5832	3
2680 ^b	157.294950	26.396518	21.42 ± 0.08	0.5843	3
2788 ^a	157.303364	26.398741	21.46 ± 0.10	0.5857	3
2685 ^b	157.297031	26.396958	21.55 ± 0.08	0.5911	3
2561 ^b	157.312173	26.395616	21.70 ± 0.09	0.5927	3
1945 ^a	157.300932	26.390149	21.72 ± 0.30	0.5830	3
2315 ^b	157.294471	26.393140	21.82 ± 0.09	0.5844	3
2653 ^b	157.302008	26.396494	21.83 ± 0.09	0.5810	3
1505 ^b	157.312688	26.386234	22.03 ± 0.10	0.5926	3
2078 ^b	157.302696	26.391330	22.06 ± 0.10	0.6026	3
2303 ^b	157.298767	26.392680	22.07 ± 0.10	0.5835	3
2903 ^b	157.310235	26.399697	22.09 ± 0.11	0.5991	3
1791 ^b	157.302474	26.388525	22.18 ± 0.11	0.5826	3
2258 ^a	157.306200	26.392746	22.19 ± 0.20	0.5969	1
1390 ^b	157.309339	26.384769	22.24 ± 0.11	0.5866	3
2415 ^b	157.296582	26.394014	22.29 ± 0.12	0.5839	3
1847 ^b	157.309245	26.389256	22.34 ± 0.12	0.5936	3
2658 ^b	157.296050	26.396134	22.34 ± 0.12	0.5888	3
2032 ^b	157.301190	26.390650	22.35 ± 0.12	0.5841	3
2421 ^b	157.302160	26.394210	22.54 ± 0.13	0.5883	3
1417 ^b	157.302030	26.385186	22.57 ± 0.13	0.5970	3
2828 ^a	157.313370	26.397935	22.63 ± 0.20	0.5924	1
2181 ^b	157.306794	26.391706	22.73 ± 0.14	0.5823	3
1324 ^b	157.310794	26.384203	22.78 ± 0.15	0.5981	1
2801 ^b	157.295337	26.397552	22.87 ± 0.15	0.5848	2
1931 ^b	157.300054	26.389811	22.93 ± 0.16	0.5775	3
1553 ^b	157.300576	26.386445	22.94 ± 0.16	0.5884	2
2186 ^a	157.303233	26.391831	22.96 ± 0.20	0.5851	3
3107 ^b	157.304071	26.400806	23.15 ± 0.17	0.5896	3
1512 ^a	157.303667	26.385967	23.16 ± 0.20	0.5908	2

Table C1
(Continued)



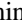
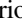







ID	R.A. (deg)	Decl. (deg)	F160W (mag)	z_{spec}	QF
2550 ^a	157.311720	26.395081	23.28 ± 0.40	0.5803	1
2468 ^a	157.304550	26.394394	23.45 ± 0.40	0.5919	1
2288 ^b	157.306805	26.392550	23.54 ± 0.21	0.5834	1
2173 ^b	157.300509	26.391560	23.94 ± 0.25	0.5863	2
2220 ^a	157.299563	26.392007	25.89 ± 0.50	0.5821	3
2973 ^b	157.305364	26.399178	26.00 ± 0.64	0.5859	3
2979 ^a	157.305288	26.399204	26.06 ± 0.40	0.5859	3
1958 ^a	157.300062	26.389995	26.22 ± 0.50	0.5819	3
663 ^b	157.298034	26.374652	21.59 ± 0.08
1185 ^b	157.307819	26.379904	21.92 ± 0.10
1301 ^b	157.323507	26.381836	20.97 ± 0.06
1446 ^b	157.313932	26.381922	22.60 ± 0.13
1523 ^b	157.303442	26.383164	21.17 ± 0.07
1527 ^b	157.320831	26.383690	19.92 ± 0.04
1645 ^b	157.313911	26.383909	21.62 ± 0.09
1701 ^b	157.314040	26.384864	21.58 ± 0.08
1878 ^b	157.286797	26.385906	22.97 ± 0.16
1958 ^b	157.291461	26.386564	22.29 ± 0.12
1974 ^b	157.314545	26.386778	22.73 ± 0.14
2257 ^b	157.293281	26.389096	20.96 ± 0.06
2374 ^b	157.324898	26.390041	22.01 ± 0.10
2930 ^b	157.314447	26.394108	19.99 ± 0.04
3281 ^b	157.285541	26.396919	21.61 ± 0.09
4015 ^b	157.293265	26.402481	21.84 ± 0.09
4033 ^b	157.306745	26.402921	22.20 ± 0.11
4040 ^b	157.295230	26.403995	19.69 ± 0.04
4396 ^b	157.304565	26.405718	22.40 ± 0.12
4435 ^b	157.298666	26.406534	21.02 ± 0.06

Notes.

^a Coordinates and F160W magnitude (and associated error) are measured with Galfit.

^b Coordinates and F160W magnitude (and associated error) are measured with SExtractor.

ORCID iDs

Ana Acebron  <https://orcid.org/0000-0003-3108-9039>
 Claudio Grillo  <https://orcid.org/0000-0002-5926-7143>
 Pietro Bergamini  <https://orcid.org/0000-0003-1383-9414>
 Amata Mercurio  <https://orcid.org/0000-0001-9261-7849>
 Piero Rosati  <https://orcid.org/0000-0002-6813-0632>
 Gabriel Bartosch Caminha  <https://orcid.org/0000-0001-6052-3274>
 Paolo Tozzi  <https://orcid.org/0000-0003-3096-9966>
 Gabriel B. Brammer  <https://orcid.org/0000-0003-2680-005X>
 Massimo Meneghetti  <https://orcid.org/0000-0003-1225-7084>
 Mario Nonino  <https://orcid.org/0000-0001-6342-9662>
 Eros Vanzella  <https://orcid.org/0000-0002-5057-135X>

References

- Acebron, A., Jullo, E., Limousin, M., et al. 2017, *MNRAS*, 470, 1809
 Akaike, H. 1974, *ITAC*, 19, 716
 Bacon, R., Accardo, M., Adjali, L., et al. 2010, *Proc. SPIE*, 7735, 773508
 Bacon, R., Vernet, J., Borisova, E., et al. 2014, *Msngr*, 157, 13
 Balestra, I., Mercurio, A., Sartoris, B., et al. 2016, *ApJS*, 224, 33
 Bender, R., Burstein, D., & Faber, S. M. 1992, *ApJ*, 399, 462
 Bergamini, P., Rosati, P., Mercurio, A., et al. 2019, *A&A*, 631, A130
 Bergamini, P., Rosati, P., Vanzella, E., et al. 2021, *A&A*, 645, A140
 Bertin, E., & Arnouts, S. 1996, *A&AS*, 117, 393
 Birrer, S., Treu, T., Rusu, C. E., et al. 2019, *MNRAS*, 484, 4726

- Bonvin, V., Chan, J. H. H., Millon, M., et al. 2018, *A&A*, 616, A183
- Caldwell, J. A. R., McIntosh, D. H., Rix, H.-W., et al. 2008, *ApJS*, 174, 136
- Caminha, G. B., Grillo, C., Rosati, P., et al. 2016, *A&A*, 587, A80
- Caminha, G. B., Grillo, C., Rosati, P., et al. 2017, *A&A*, 607, A93
- Caminha, G. B., Rosati, P., Grillo, C., et al. 2019, *A&A*, 632, A36
- Cappellari, M. 2017, *MNRAS*, 466, 798
- Cappellari, M., & Emsellem, E. 2004, *PASP*, 116, 138
- Cappellari, M., Scott, N., Alatalo, K., et al. 2013, *MNRAS*, 432, 1709
- Cerny, C., Sharon, K., Andrade-Santos, F., et al. 2018, *ApJ*, 859, 159
- Chirivì, G., Suyu, S. H., Grillo, C., et al. 2018, *A&A*, 614, A8
- Courbin, F., Bonvin, V., Buckley-Geer, E., et al. 2018, *A&A*, 609, A71
- Elíasdóttir, Á., Limousin, M., Richard, J., et al. 2007, arXiv:0710.5636
- Faber, S. M., Dressler, A., Davies, R. L., et al. 1987, in *Nearly Normal Galaxies. From the Planck Time to the Present*, ed. S. M. Faber (New York: Springer-Verlag), 175
- Fohlmeister, J., Kochanek, C. S., Falco, E. E., et al. 2007, *ApJ*, 662, 62
- Fohlmeister, J., Kochanek, C. S., Falco, E. E., et al. 2013, *ApJ*, 764, 186
- Freedman, W. L., Madore, B. F., Hoyt, T., et al. 2020, *ApJ*, 891, 57
- Ghosh, A., Williams, L. L. R., & Liesenborgs, J. 2021, *MNRAS*, 506, 6144
- Goobar, A., Amanullah, R., Kulkarni, S. R., et al. 2017, *Sci*, 356, 291
- Granata, G., Mercurio, A., Grillo, C., et al. 2021, arXiv:2107.09079
- Grillo, C., Karman, W., Suyu, S. H., et al. 2016, *ApJ*, 822, 78
- Grillo, C., Rosati, P., Suyu, S. H., et al. 2018, *ApJ*, 860, 94
- Grillo, C., Rosati, P., Suyu, S. H., et al. 2020, *ApJ*, 898, 87
- Grillo, C., Suyu, S. H., Rosati, P., et al. 2015, *ApJ*, 800, 38
- Inada, N., Oguri, M., Morokuma, T., et al. 2006, *ApJL*, 653, L97
- Inada, N., Oguri, M., Pindor, B., et al. 2003, *Natur*, 426, 810
- Inada, N., Oguri, M., Shin, M.-S., et al. 2012, *AJ*, 143, 119
- Jauzac, M., Eckert, D., Schwinn, J., et al. 2016, *MNRAS*, 463, 3876
- Jauzac, M., Klein, B., Kneib, J.-P., et al. 2021, *MNRAS*, 508, 1206
- Jauzac, M., Mahler, G., Edge, A. C., et al. 2019, *MNRAS*, 483, 3082
- Johnson, T. L., & Sharon, K. 2016, *ApJ*, 832, 82
- Jullo, E., Kneib, J. P., Limousin, M., et al. 2007, *NJPh*, 9, 447
- Kawamata, R., Oguri, M., Ishigaki, M., Shimasaku, K., & Ouchi, M. 2016, *ApJ*, 819, 114
- Keeton, C. R., & Moustakas, L. A. 2009, *ApJ*, 699, 1720
- Kelly, P. L., Rodney, S. A., Treu, T., et al. 2015, *Sci*, 347, 1123
- Kelly, P. L., Rodney, S. A., Treu, T., et al. 2016, *ApJL*, 819, L8
- Kneib, J. P., Ellis, R. S., Smail, I., Couch, W. J., & Sharples, R. M. 1996, *ApJ*, 471, 643
- Lagattuta, D. J., Richard, J., Bauer, F. E., et al. 2019, *MNRAS*, 485, 3738
- Limousin, M., Kneib, J.-P., & Natarajan, P. 2005, *MNRAS*, 356, 309
- Limousin, M., Richard, J., Jullo, E., et al. 2016, *A&A*, 588, A99
- Lotz, J. M., Koekemoer, A., Coe, D., et al. 2017, *ApJ*, 837, 97
- Mahler, G., Richard, J., Clément, B., et al. 2018, *MNRAS*, 473, 663
- McCully, C., Keeton, C. R., Wong, K. C., & Zabludoff, A. I. 2017, *ApJ*, 836, 141
- Meneghetti, M., Natarajan, P., Coe, D., et al. 2017, *MNRAS*, 472, 3177
- Monna, A., Seitz, S., Geller, M. J., et al. 2017, *MNRAS*, 465, 4589
- Monna, A., Seitz, S., Zitrin, A., et al. 2015, *MNRAS*, 447, 1224
- Oguri, M. 2007, *ApJ*, 660, 1
- Oguri, M., Inada, N., Pindor, B., et al. 2006, *AJ*, 132, 999
- Oguri, M., Ofek, E. O., Inada, N., et al. 2008, *ApJL*, 676, L1
- Oguri, M., Schrabback, T., Jullo, E., et al. 2013, *MNRAS*, 429, 482
- Ota, N., Oguri, M., Dai, X., et al. 2012, *ApJ*, 758, 26
- Peng, C. Y., Ho, L. C., Impey, C. D., & Rix, H.-W. 2010, *AJ*, 139, 2097
- Pignataro, G. V., Bergamini, P., Meneghetti, M., et al. 2021, *A&A*, 655, A81
- Planck Collaboration, Aghanim, N., Akrami, Y., et al. 2020, *A&A*, 641, A6
- Refsdal, S. 1964, *MNRAS*, 128, 307
- Remolina González, J. D., Sharon, K., & Mahler, G. 2018, *ApJ*, 863, 60
- Rescigno, U., Grillo, C., Lombardi, M., et al. 2020, *A&A*, 635, A98
- Richard, J., Patricio, V., Martinez, J., et al. 2015, *MNRAS*, 446, L16
- Riello, M., De Angeli, F., Evans, D. W., et al. 2021, *A&A*, 649, A3
- Riess, A. G., Casertano, S., Yuan, W., et al. 2021, *ApJL*, 908, L6
- Riess, A. G., Casertano, S., Yuan, W., Macri, L. M., & Scolnic, D. 2019, *ApJ*, 876, 85
- Rix, H.-W., Barden, M., Beckwith, S. V. W., et al. 2004, *ApJS*, 152, 163
- Rodney, S. A., Brammer, G. B., Pierel, J. D. R., et al. 2021, *NatAs*, 5, 1118
- Rodney, S. A., Strolger, L. G., Kelly, P. L., et al. 2016, *ApJ*, 820, 50
- Rojas, K., Motta, V., Mediavilla, E., et al. 2020, *ApJ*, 890, 3
- Schwarz, G. 1978, *AnSta*, 6, 461
- Sharon, K., Bayliss, M. B., Dahle, H., et al. 2017, *ApJ*, 835, 5
- Sluse, D., Rusu, C. E., Fassnacht, C. D., et al. 2019, *MNRAS*, 490, 613
- Soto, K. T., Lilly, S. J., Bacon, R., Richard, J., & Conseil, S. 2016, *MNRAS*, 458, 3210
- Suyu, S. H., Bonvin, V., Courbin, F., et al. 2017, *MNRAS*, 468, 2590
- Suyu, S. H., & Halkola, A. 2010, *A&A*, 524, A94
- Suyu, S. H., Hensel, S. W., McKean, J. P., et al. 2012, *ApJ*, 750, 10
- Tewes, M., Courbin, F., & Meylan, G. 2013, *A&A*, 553, A120
- Treu, T., Brammer, G., Diego, J. M., et al. 2016, *ApJ*, 817, 60
- Verde, L., Treu, T., & Riess, A. G. 2019, *NatAs*, 3, 891
- Weilbacher, P. M., Palsa, R., Streicher, O., et al. 2020, *A&A*, 641, A28
- Wong, K. C., Suyu, S. H., Chen, G. C. F., et al. 2020, *MNRAS*, 498, 1420
- York, D. G., Adelman, J., Anderson, J. E., Jr., et al. 2000, *AJ*, 120, 1579